



Evaluation of residual stresses in a pipe-to-plate welded joint by means of uncoupled thermal-structural simulation and experimental tests

Andrea Chiocca*, Francesco Frendo, Leonardo Bertini

Department of Civil and Industrial Engineering, University of Pisa, Largo Lucio Lazzarino 2, 56122 Pisa, Italy



ARTICLE INFO

Keywords:

Residual stresses
Relaxed strains
Thermal-structural analysis
Welding
S355
Elastic-plastic material properties

ABSTRACT

A deep knowledge of the production process is needed, in order to achieve quality and safety requirements in a component. In this context, residual stresses play an important role, especially in welded structures. The present work deals with the assessment of residual stresses in a S355JR carbon steel pipe-to-plate welded joint. Both numerical simulations and experimental tests were employed in order to gain wide-ranging knowledge. Numerical simulations were performed with the software Ansys® through an uncoupled (one-way coupling) thermal-structural simulation in order to evaluate the stress, strain and temperature at each node of the finite element model for each phase of the simulation. Temperature-dependent elastic-plastic material properties were adopted in combination with the *element birth & death* method, necessary to simulate the welding process. Two numerical weld seam solidification methods were employed and discussed, in terms of expected results and simulation performances. The obtained numerical results were compared with experimental data of relaxed radial strains measured nearby the weld seam.

1. Introduction

Residual tensile stresses are often degrading for the integrity and durability of a component; for this reason, their study and evaluation should be recommended starting from the design phase. Residual stresses are commonly associated with unexpected failures and dimensional inaccuracies. In particular, they can affect a component strength, by reducing the strain resistance [1], the fatigue life [2] and by promoting stress-corrosion failures [3]. Sometimes, residual compressive stresses are intentionally introduced, in order to increase the strength of a part (e.g. shot peening and plastic deformation used to increase the fatigue endurance of automotive helical springs [4]). For the optimized design of a component, for example aimed at reducing the weight and/or costs (i.e. lightweight design), the accurate knowledge of the state of stress, including residual stresses, is mandatory.

Residual stresses may originate from different mechanisms; they may be associated to the production process (e.g. plastic deformations, thermal treatments and phase transformations) or the in-service life (e.g. temperature distributions or load induced plastic deformations). During the welding process many of those mechanisms occur simultaneously.

The experimental evaluation of residual stresses is always obtained by indirect ways [5]. Some methods are based on the elastic deformation or displacement produced by the removal of a given (stressed) material volume: the most commonly employed methods include destructive

techniques (e.g. sectioning method [6]) or semi-destructive techniques (e.g. hole drilling [7]); other, non-destructive, methods are based on the alteration of wave transmission properties induced by the crystal lattice deformation associated to residual stresses (e.g. neutron diffraction [8] and ultrasound [9,10]).

Unfortunately, through experimental tests it is difficult to obtain complete and statistically relevant results [11,12] and the finite element analysis (FEA) has become an increasingly used technique for predicting the overall stress state. In facts, in the last decades, numerical methods have been applied for predicting residual stresses resulting from manufacturing processes such as casting [13–17], welding [18–29] and additive manufacturing [30–35]. This technique allows easy computing of residual stresses, although it has some limitations due to the large number of parameters involved in the process (e.g. transient behavior, heat sources, phase transformations, temperature distribution, temperature dependent materials properties, etc.) and results may be biased by the simplifications introduced in the model (e.g. simplified component geometry and material properties), in order to make it computationally efficient.

A valid application of the FEA lies in understanding how different input parameters affect the simulation results. In this way FEA becomes a valuable tool, easily accessible and with less economic effort than experimental tests, which can be time consuming and expensive.

* Corresponding author.

E-mail addresses: andrea.chiocca@phd.unipi.it (A. Chiocca), francesco.frendo@unipi.it (F. Frendo), leonardo.bertini@unipi.it (L. Bertini).

Nomenclature

GMAW	Gas Metal Arc Welding
$R_{p0.2}$	Yield strength
Δr_{ext}	Radial distance from strain gauge grid center to weld toe
$\Delta\theta$	Angular step between strain gauges
R_m	Ultimate tensile strength
d	Incremental hole diameter
δ	Incremental hole depth
E	Young's modulus
G	Tangential modulus
H	Hardening law coefficient
N	Hardening exponent
σ_{rr}	Residual radial stresses
$\sigma_{\theta\theta}$	Residual hoop stresses
ε_p	Plastic strain
ε_{th}	Thermal strain
ε_{Rrr}	Relaxed radial strain
α	Coefficient of thermal expansion
v	Poisson's ratio
HV	Vickers hardness
k	Conductivity
c_p	Specific heat
l_c	Shell characteristic length
ρ	Density
Q_{int}	Internal heat source rate
x, y, z	Cartesian coordinate system
T	Temperature
r, θ, z	Cylindrical coordinate system
t	Time
t_i	Simulation time at i-th substep
FEA	Finite Element Analysis
FEM	Finite Element Model
CIT	Constant Initial Temperature
RWP	Representative Welding Process numerical model
T_i	Calibration parameter of the Constant Initial Temperature model
T_r	Room temperature
T_m	Melting temperature of the base material
T_{ref}	Reference temperature at zero initial thermal strain
σ	Total stress
σ_y	Initial yield stress

Several studies have been found relative to finite element analysis of residual stress, both for bi- and three-dimensional problems. Ferro et al. [36] studied the effect of weld passes on the residual stress field for a butt-welded joint, Zhou et al. [37] analysed the influence of residual stresses on creep behavior for a multi-pass circular weld, Barsoum et al. [2] obtained a forecast of the stresses that will later be incorporated into a crack growth model and Wang [38] computed residual stresses in a welded specimen for later use them in a multiaxial fatigue assessment study. All the previously described researches provide a satisfactory description of the current state of the art with regard to thermal-structural simulations. Specifically for the thermal analysis, heat sources such as Goldak's double-ellipsoid or volumetric heat flux were used, both of which depend on the welding process parameters. During the subsequent structural simulation, the previously computed temperatures were applied as a thermal load on FE-model elements.

In the present work a comprehensive analysis of residual stress on a pipe-to-plate welded joint is carried out by both numerical and experimental analyses. An uncoupled thermal-structural simulation has been used in Ansys® FE software; as the displacements obtained during welding are limited and have a negligible influence on the thermal distribu-

tion, the uncoupled formulation is acceptable in this context [39]. This simulation model is commonly used for welding processes, as already described by different authors [40–44]. The welding process is replicated by means of the *birth & death* technique¹, combined with a heat source model (i.e. constant initial temperature). The heat source is, in this case, independent from the process parameters, as it is solely related to a fictitious initial temperature obtainable by comparison with experimental data. The structural analysis, on the other hand, ensures an accurate representation of the local stiffness of the component during the welding process. Numerical results were corroborated by comparison with several experimental data.

The adopted heat source model has already been validated in a previous work from the same authors [45], while the structural analysis was verified through comparison with relaxed strains, which were experimentally obtained by an incremental cutting process performed on the bottom of the plate [46].

2. Material and methods

The specimen, shown in Fig. 1, includes a tube reinforced internally through a circular plate and then welded to a flange by means of a single pass of gas metal arc welding (GMAW) through a TransPlusSynergic 4000 machine. The welding process was carried out manually, by maintaining the welding torch stationary and using a rotating bench whose speed was controlled, as required, by the operator. As a result, a high repeatability of the welding process was guaranteed. The welding process parameters, used as benchmark for all the simulations, are given in Table 1; a cross-section of the weld seam is given in Fig. 2. Both the plate and the tube were made by structural steel S355JR, while the filler material was an EN ISO 14341-A G 464. The chemical compositions of both the base and filler materials are given in Tables 2 and 3 respectively, while the mechanical properties of the base material are shown in Table 4, where $R_{p0.2}$ is the yield strength, R_m is the tensile strength, E is the Young's modulus, G is the tangential modulus, v is the Poisson's ratio and HV_{10} is the Vickers microhardness for an approximate test force of 10kgf.

As shown in Fig. 1, the tube has an internal diameter of 44mm and a wall thickness of 10mm, while the plate to which it is welded to, is quadrangular, with 190mm edge length and 25mm of thickness. Four holes, with a diameter of 21mm, were symmetrically drilled into the plate. The holes as well as the internal volume created by the circular support were necessary for a fatigue assessment investigation of the welded joint. Likewise, a central gas thread of 1/4 of inches (G1/4 of standard ISO 7-1:1994) was used to pressurize the lower chamber and detect a through-the-thickness crack during fatigue testing [47–50].

An incremental cutting procedure was performed on the bottom of the plate in order to acquire a series of experimental relaxed strains, representative of the residual stress state in the welded region (i.e. Fig. 3a). The process involved drilling the base of the plate, slowly increasing diameter and depth dimension of the hole. Two holes of different diameters and depths were machined. The first is a through hole of 42 mm in diameter while the second is an incremental hole, 100 mm in diameter and total depth of 20 mm; this procedure is schematized in a simplified way in Fig. 4.

The experimental procedure was then reproduced by a numerical simulation in order to validate the overall numerical analysis described before (i.e. Fig. 3b). A similar strategy of element deactivation has been implemented by Salerno et al. [51], applied for material removal preceding a repair welding process. However, the removed material volume made by Salerno was negligible compared to the overall volume of the component, leading to a negligible difference within the residual stress

¹ This method requires the deactivation and reactivation of the bead elements, by multiplying the stiffness matrix with a coefficient close to zero or one respectively.

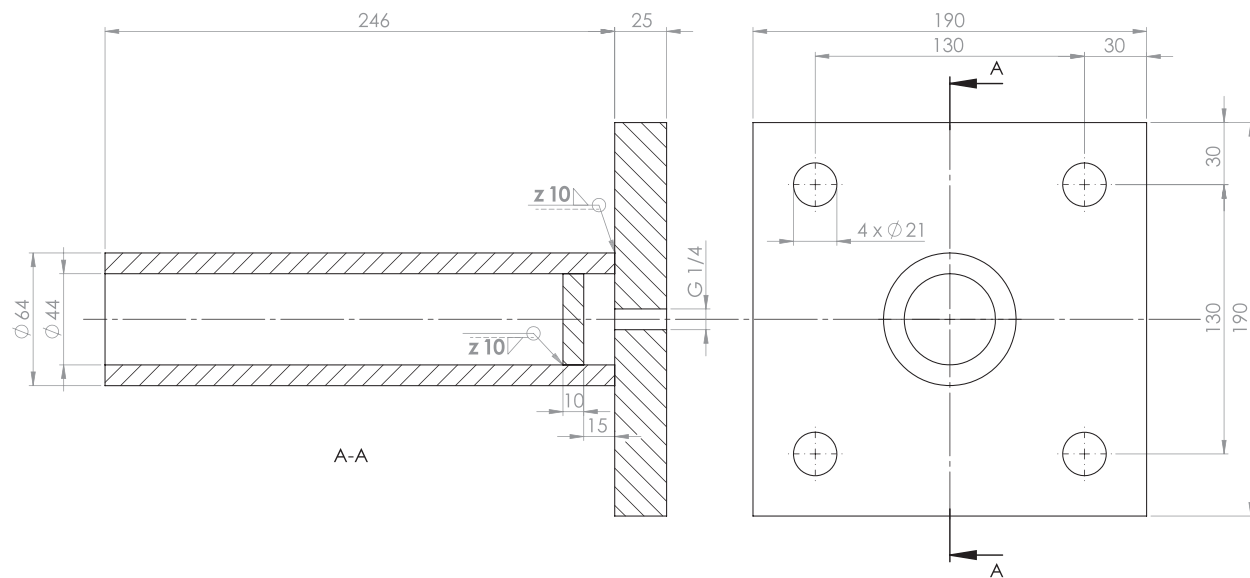


Fig. 1. Technical drawing of the pipe-to-plate welded joint with dimensions in millimetres and welding representation according to ISO 22553:1992

Table 1
Welding process parameters

Current (A)	Voltage (V)	Welding Time (s)	Welding Speed (mm s^{-1})
211	25	75	2.7
Filler material	Wire diameter (mm)	Shielding gas	Gas flowrate (mm s^{-1})
EN ISO 14341-A G 464	1.20	82% Ar 18% CO ₂	0.62

Fig. 2. Image of the investigated specimen with a micrograph of the weld seam

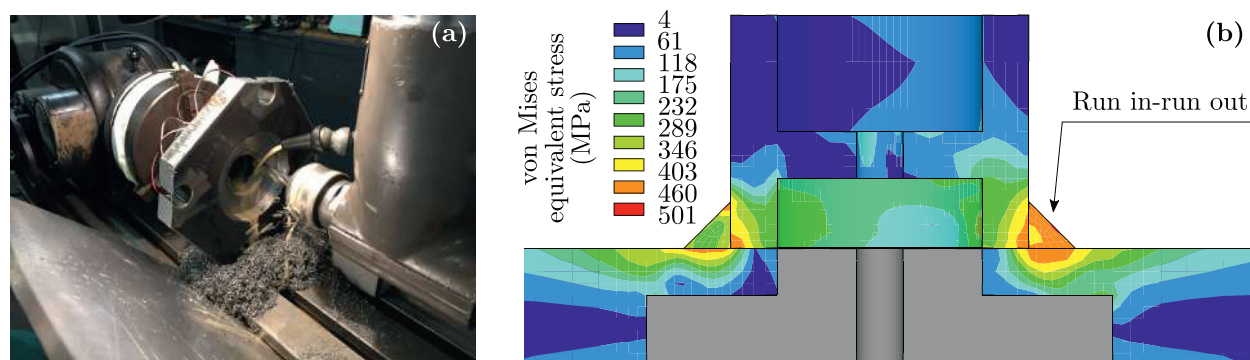


Fig. 3. Experimental machining of the bottom part of the specimen plate (a), numerical simulation of the incremental cutting process (b)

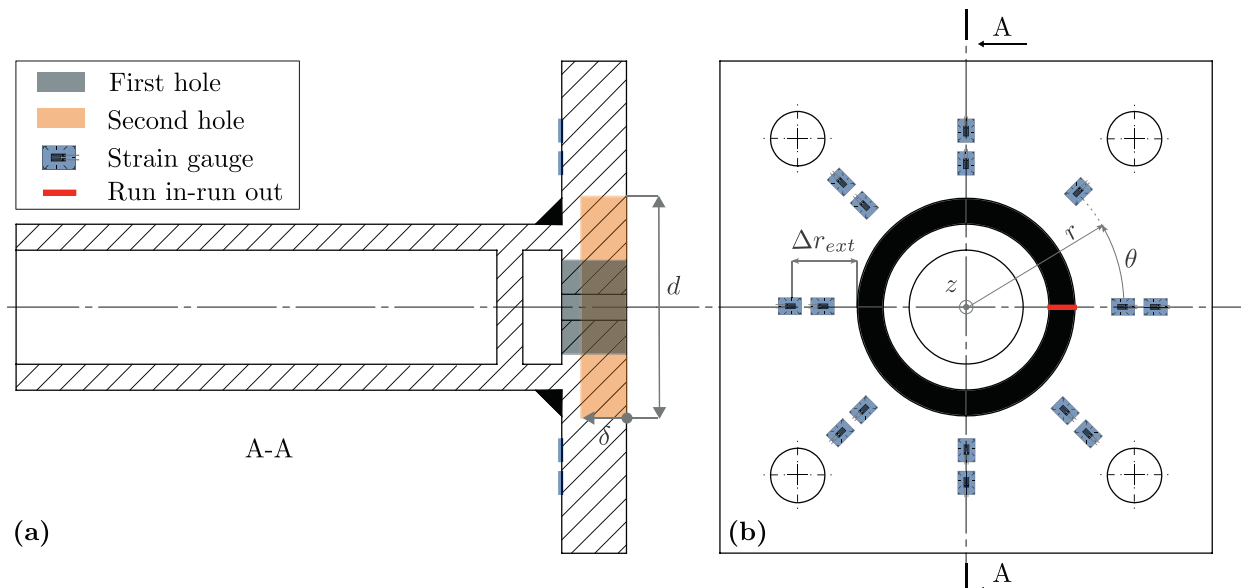


Fig. 4. Incremental hole drilling process used to detect relaxed strains (a) and qualitative layout of the strain gauges (b)

Table 2
Chemical composition (wt%) of S355JR structural steel

C	Si	Mn	P	S	N	Cu
0.24	0.55	1.6	0.035	0.035	0.012	0.55

Table 3
Chemical composition (wt%) of EN ISO 14341-A G 464
filler material

C	Si	Mn	Cu
0.065–0.08	0.90–1.00	1.60–1.70	max. 0.30

Table 4
Mechanical properties of S355JR structural steel at room temperature

$R_{p0.2}$ (MPa)	R_m (MPa)	E (GPa)	G (GPa)	ν	HV_{10}
355	470	206	77.4	0.3	180

distribution caused by the original joining process. On the contrary, in our study the interest lies in obtaining a significant difference in the residual stress state between the drilled and non-drilled component in order to allow strain gauges to operate well beyond their background noise, albeit within their maximum tolerance.

The step-based cutting process was implemented to control the acquired result and be confident about the reading of strain gauges.

3. Finite element analysis

Uncoupled thermal-structural simulations were performed by using the software Ansys® vers. 19.2. As already stated, an uncoupled simulation was adopted to limit the computational effort, given the complex nature of the investigated process. The thermal problem was firstly solved and then the results, in terms of nodal temperatures, were used in the structural analysis as thermal loads. The analysis is transient and capable of describing how the temperature history affects the structural results, mainly, through the use of temperature-dependent material properties. In general, the simulation is divided into three steps, to

be sequentially solved, in order to reproduce the entire² process: thermal analysis, structural analysis and incremental hole drilling analysis. Each step is described in more details in the following. A fully three-dimensional model was adopted since the thermal load during the welding process cannot be considered axisymmetric. Stresses and strains produced through the welding process ultimately depend on the hoop coordinate [2], because heat is transferred gradually along the angular direction and this results in a non uniform deformation of the component. A residual stresses investigation regarding two-dimensional and three-dimensional models have been reported and compared in a preliminary work made by the authors [52]; the difference in employing linear-elastic or elastic-plastic material properties were also discussed in that work.

3.1. Thermal analysis

The thermal simulation of the welding process was carried out and the temperature time-history at each node of the FE model was obtained (this analysis is aimed at achieving only the temperature time-history due to the welding process, without considering the structural behavior). The thermal analysis follows the thermal equilibrium Eq. (1):

$$k \left(\frac{\partial^2 T}{\partial x^2} + \frac{\partial^2 T}{\partial y^2} + \frac{\partial^2 T}{\partial z^2} \right) + Q_{int} = \rho c_p \frac{\partial T}{\partial t}, \quad (1)$$

where Q_{int} is the internal heat source rate, and k , c_p , and ρ are the conductivity, specific heat capacity and density of the material, respectively. The load commonly used in this context is a temperature or a thermal heat flux (e.g. constant initial temperature [45], gaussian [53] or double ellipsoidal [54]). Generally, the load parameters are set depending on the welding process, material and joint geometry. The heat source employed during the thermal simulation is a *constant initial temperature* (*CIT*) imposed to a given material volume, representing the melt pool. The reader can refer to Chiocca et al. [45] for a more detailed discussion of this method and for general comparison between different thermal sources, which can be employed into an FE analysis. Overall, the proposed thermal model intends to be easier to be implemented, if compared to the well-known Goldak double ellipsoid, which requires

² The whole process is constituted by welding the tube to the top surface of the plate and then incrementally drilling a hole from the bottom surface of the plate, in order to get the relaxed strains.

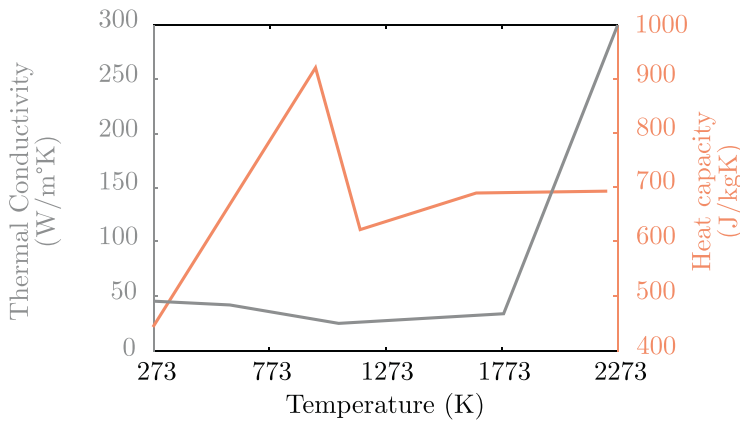


Fig. 5. Temperature dependent thermal material properties of S355 steel derived from [55]

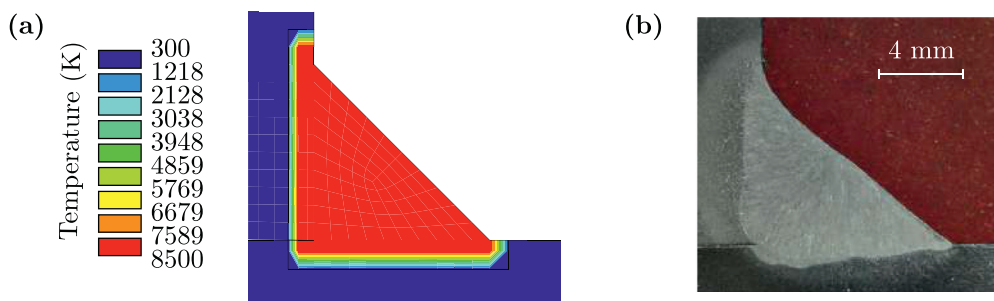


Fig. 6. Weld seam elements activation at the initial temperature $T_i = 8500\text{K}$ for implementing the constant initial temperature method (a). Cross section of the weld seam (b)

an extreme and accurate calibration phase. The CIT method is relatively simple, depending on a single calibration parameter (T_i). It is worth noting that this method is aimed at providing a reasonably accurate reproduction of the temperature distribution surrounding the weld seam; the actual thermal behavior (which is also influenced by phase transformations and other metallurgical phenomena) inside the weld seam cannot be reproduced by this model.

The SOLID70 element was used for the thermal analysis in Ansys*. It is a brick element with eight nodes and temperature as the only degree of freedom. The thermal properties of the material were taken from Zhu et al. [55] (Fig. 5). The thermal conductivity and heat capacity were assumed as temperature-dependent material properties. No metallurgical phenomena have been modelled, however, on the basis of Deng [40], Cho and Kim [56], Caprace et al. [57], phase transformations seem to have no significant influence on the mechanism of residual stress generation for low carbon steel.

The simulated molten pool shape is commonly calibrated by means of experimental comparison, varying the thermal conductivity at high temperatures. Due to the difficulty in experimentally validating this quantity, a fictitious thermal conductivity at 2273K was implemented based on Zhu et al. [55], which employed the same welding process and material here described. The heat convection and emissivity coefficients were considered as constant with values of $20\text{Wm}^{-2}\text{K}^{-1}$ and 0.79, respectively. This hypothesis was verified a posteriori by a sensitivity analysis performed on these parameters, as described in [45]. Regarding the bottom surface of the plate, the heat convection coefficient was increased to a value of $500\text{Wm}^{-2}\text{K}^{-1}$ because of the sink effect resulting from the contact between the specimen and the metallic support during the welding process; the convection value has been considered suitable as comparable to the one used in [58].

Initial conditions are represented by an uniform temperature of the whole component, equal to the room temperature $T_r = 300\text{K}$. The element *birth & death* technique was used to deactivate and subsequently, at given times, reactivate the elements belonging to the weld seam with a given initial temperature. The elements that needed to be deactivated and then reactivated were determined directly from a cross section of

the weld seam, as shown in Fig. 6. This method has only a "fictitious" initial temperature (T_i) as setting parameter and was proven to be able to reproduce the temperature distribution at the nodes, with very good agreement, even if compared to more complex methods. The fictitious initial temperature needs to be set for every specific joint geometry, welding process and component material through the comparison with experimental data. Specifically, for the analysed case $T_i = 8500\text{K}$ as reported by the authors in [45].

It is worth noting that, although the CIT method may appear approximate compared to other methods (i.e. Goldak double ellipsoid, Gaussian heat flux, constant heat flux), it is designed to resemble what occurs during arc-based welding processes involving filler material. In processes with added filler material, at a certain process time t_i , molten and base materials come into contact. On the contrary, in processes such as additive manufacturing or beam-based welding processes, base material is directly melted. Therefore, in this case, thermal profile better resembles the one described by models such as Goldak double ellipsoid or Gaussian heat flux.

In terms of numerical performances, the implementation of the CIT model required 1069s of elapsed time, spent for computing the solution on a workstation endowed with four physical cores running in parallel and 16 GB of RAM available.

3.2. Structural analysis

After the thermal analysis the welding process was then structurally reproduced. The load, obtained as a time-temperature binary data file resulting from the thermal simulation, was applied to the nodes of the FE model. In this stage, the structural stresses and strains over time are computed starting from the temperature evolution. The structural problem is, actually, time-dependent and, as explained in [39], the cause is mainly due to the material plasticity, time-history of the thermal load and the time-varying FE domain. Due to the low yield stress of the material at high temperature, a significant mesh distortion may cause a bad numerical convergence of the solution. To overcome this issue, remeshing operations or gradual application of the thermal load (e.g. by

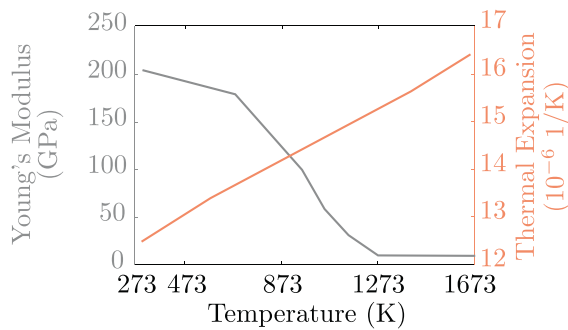


Fig. 7. Temperature dependant structural material properties of S355 steel acquired from [55]

increasing the number of substeps for the solution phase) can be alternatively used.

In this case, the number of substeps was incremented until a satisfactory solution was achieved.

Temperature dependent material properties for the structural analysis were derived from Zhu et al. [55] and are presented in Fig. 7. The linear elastic stress-strain model is described through a temperature dependent Young's modulus (E) and a constant Poisson's ratio ($\nu = 0.3$). Instead, the elastic-plastic stress-strain relationship follows Eq. 2

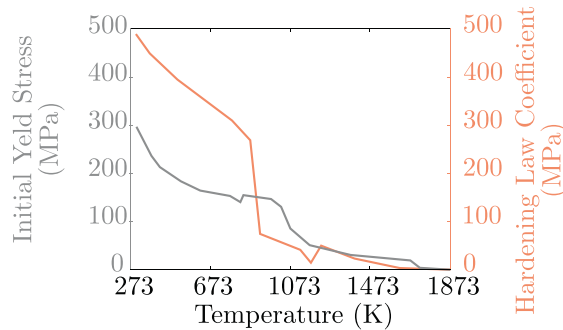
$$\sigma = \sigma_y + H(\varepsilon_p)^N \quad (2)$$

where σ is the total stress, σ_y is the yield stress, H is the hardening law coefficient, ε_p is the plastic strain and N is the hardening exponent that in this case was assumed as constant ($N = 0.25$). A satisfactory convergence of the numerical stress/strain results was obtained implementing the material properties of Fig. 7 up to a maximum temperature of 1273K. A reasonable explanation for this, is that negligible changes in the material stiffness take place beyond a given (high) temperature. For temperatures higher than 1273K, material properties like the Young's modulus and initial yield stress are almost negligible, meaning that the material above that temperature cannot bring a significant contribution in terms of stiffness.

The same mesh grid was applied for both thermal and structural analyses, to correctly implement the thermal load in the right nodal position. Elements were updated, from thermal to mechanical element type; the eight-node SOLID185 element was used, with three degrees of freedom (the displacements in x, y and z directions) at each node. As boundary conditions, displacements of nodes on the upper surface of the tube (far away from the weld) were constrained. Although this did not reflect the real bound used during the welding process, it allows the specimen to freely deform as it happens during the real process. Any edge effect caused by the imposed constraint did not affect the stress and strain fields in proximity of the weld seam (it may alter the solution nearby a cylindrical area defined by the shell characteristic lengths³).

Similarly to the thermal simulation, also in the structural analysis the element *birth & death* method was implemented to better reproduce the component behavior during the welding process.

Two methods were employed, i.e. the *classic approach* and a *representative welding process* (*RWP* in the following). According to the *classic approach* all elements belonging to a section of the molten bead are sequentially activated for the structural analysis, independently from their temperature at that given time. With the *RWP* method, elements having a temperature higher than the melting point ($T_m = 1760\text{K}$) are deactivated, while elements whose temperature drop below the melting point are reactivated. The melting point can be defined as the temperature for isothermal solidification or the liquidus or solidus temperature otherwise (given the inherent assumptions of a finite element problem,



there is a negligible difference in the choice of T_m for classic steel alloys, as long as it remains within the range described above).

Fig. 8 schematically describes both the *classic* and the *RWP* methods applied to solve the structural problem, showing an example of weld bead cooling sequence after applying the *CIT* thermal model. Fig. 8a and b, give an overview of the active elements at a generic welding time t_i . As a matter of fact, from Fig. 8c and d, the difference in the cooling sequence between the two models can be identified. According to the *classic* method, elements are deactivated/reactivated solely based on the simulation time, whereas, according to the *RWP* method, the element activation is based on the element temperature. In Fig. 8d, it is possible to identify a sequential activation of the elements with temperature lower than the melting point. The result thus obtained represents what expected from the solidification of a pool of molten metal during the welding process. This process is repeated for every iteration of metal deposition, leading to a quite different structural result compared to the *classic* method. It can be observed, for instance, in Fig. 8d, that a colder layer is created during the process, on the surface of the molten material, caused by the elevated thermal convection between the hot metal and the environment.

In order to simplify the model understanding, a graphical flowchart of the code sequence used to implement the *RWP* is shown in Fig. 9, with reference to the generic simulation time t_i .

The importance of using this formulation is related with the different stiffness that the specimen experiences during the process, which can lead to different residual stress fields at the end of the simulation. Furthermore, this method allows to set different *temperature at zero thermal strain* for the molten pool and base material, according to the following relationship used in Ansys® software:

$$\varepsilon_{th} = \alpha(T - T_{ref}) \quad (3)$$

where ε_{th} represents the thermal strain, α is the coefficient of thermal expansion, T is the instantaneous temperature of the element, while T_{ref} is the reference *temperature at zero thermal strain*; this temperature was set to 1760K for the elements belonging to the weld seam and 300K for all the others. The structural solution and especially the simulation of the molten metal deposition are highly dependent on the mesh size. However, while it is straightforward to achieve convergence for structural and thermal results (e.g. h-convergence method), the same outcome was not attainable with regard to the molten metal deposition process (*RWP*). The problem arose trying to simulate a continuous-based process (i.e. welding process), through a discrete model (i.e. *CIT* method). Unlike the methods based on thermal heat flux, the *CIT* model is mesh size dependent (i.e. the volume of material activated at temperature T_i varies depending on the number of selected elements). The benchmark for the convergence of both mesh size and the volume of activated elements during the thermal simulation was considered based on the convergence of both thermal (i.e. temperature) and mechanical (i.e. stress and strain) results. It was achieved with an average element dimension of approximately 1mm in the proximity of the weld bead and the activa-

³ $I_c = \frac{\sqrt{Rh}}{\sqrt{3}(1-\nu^2)} = 13.65\text{mm}$, where $R = 27\text{mm}$ is the mean tube radius, $h = 10\text{mm}$ is the tube thickness and $\nu = 0.3$ is the Poisson's ratio

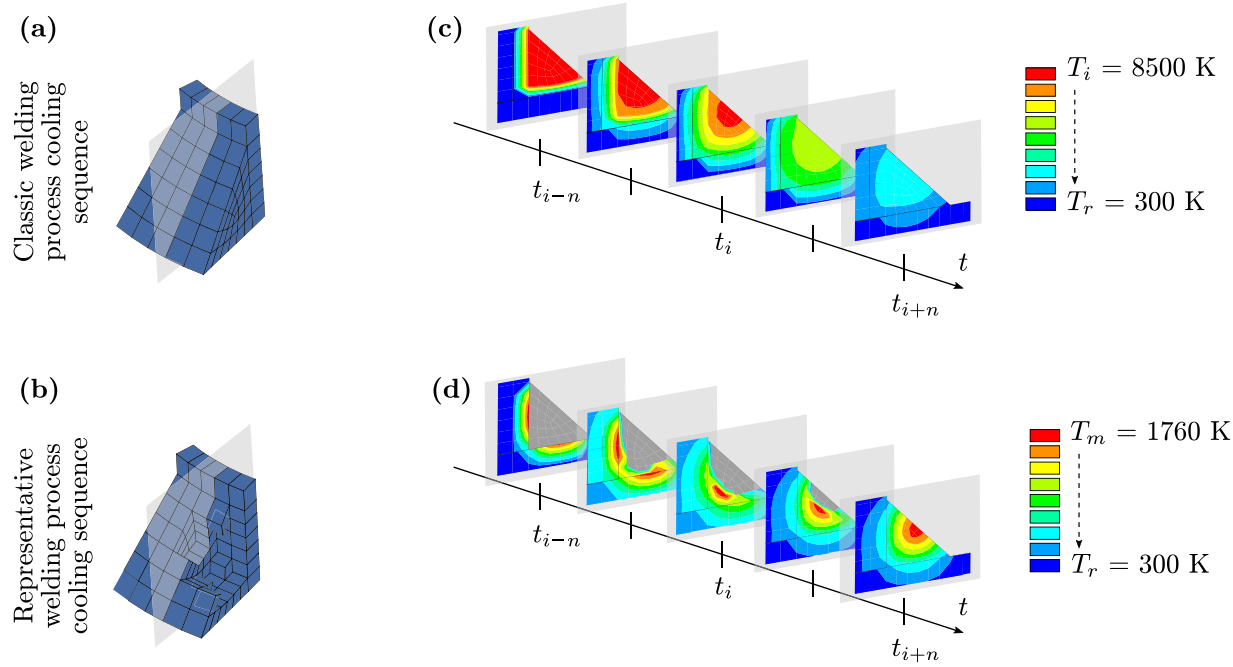


Fig. 8. Weld seam volume segment for the *classic* (a) and *RWP* (b) methods; cooling sequence of a weld seam section during the structural simulation for the *classic* (c) and *RWP* (d) methods

tion of elements contained in a volume defined by a 0.1 radiant arc of the weld seam (i.e. the weld seam segments of Fig. 8a and b).

3.3. Incremental cutting numerical model

The incrementally cutting process was simulated by FEA through a sequential deactivation of some elements. No additional inputs were assigned to the numerical model, since the structural simulation results achieved in the previous step were used as initial conditions. The finite element model is kept unchanged compared to the structural simulation discussed above. It is worth noting that the FE-model requires an initial ad-hoc design in order to perform the incremental cutting phase. Indeed, a component sub-volume partition is required, allowing a mesh generation that matches the holes diameter and depth, to be able to properly simulate the right material volume removal.

Another aspect to keep in mind is the correct location of the nodes in the right strain gauge reading positions. This is recommended to prevent the need to interpolate the solution between the nodes in the nearby positions. This technique allows the experimental determination of the relaxed strain in specific spots for direct comparison through strain gauges, as described below in Section 4. The cutting process is easily reproduced numerically, throughout the element *birth & death* technique. The incremental cutting process simulation provides a straightforward comparison of strains thus measured, both numerically and experimentally. The evaluation of the stress state is achieved directly via the FE-analysis. In terms of numerical performances, the *classic* and *RWP* methods required similar simulation time of respectively 29785s and 32639s, with regard four physical cores running parallel and 16 GB of RAM available. The time spent in computing the solution was, in this case, considerably greater compared to the thermal simulation.

4. Relaxed strain experimental measurements

Relaxed radial strain measurements were experimentally obtained in order to validate the numerical results derived from the simulation previously discussed. Strain gauges were placed at different radial (Δr_{ext}) and angular (θ) coordinates to map the radial strain as a function of the two reference parameters i.e. the hole diameter (d) and hole depth (δ).

Table 5

Summary of experimental test set-up for relaxed radial strain measurements

Name	Strain gauges qty.	Grid length (mm)	Δr_{ext} (mm)	$\Delta\theta$ ($^{\circ}$)
Test-1	8	1.5	6.5/9/13	90
Test-2	6	1.5	6.5/9/13	90
Test-3	12	1.5	6.5	30
Test-4	12	1.5/0.6	6.5	15/6

Fig. 4 shows how both Δr_{ext} and θ refer to the center of the positioning grid of strain gauges, which is required as numerical results consider this point when computing data from the FE-model.

Linear strain gauges were employed with measuring grid length of 1.5mm and 0.6mm and with nominal resistance of 120 Ω (i.e. 1-LY1x-1.5/120 and 1-LY1x-0.6/120 from HBM), while the data acquisition system used was a *Model 5100B Scanner* from StrainSmart. Strain gauges with a grid length of 1.5mm were positioned at an angular step of $\Delta\theta > 15^{\circ}$, while strain gauges with a grid length of 0.6mm were positioned at $\Delta\theta = 6^{\circ}$ of angular step. Specifically, strain gauges with a grid length of 0.6mm were used for localized strain measurements, located in the area opposite to the run in-run out point (start-end point of the single pass arc weld), to get an indication of the intrinsic variability of strain measurements, as explained later in Section 5.2. Different strain gauge set-ups are shown in Table 5, where $\Delta\theta$ is the angular step between strain gauges and Δr_{ext} is the distance between the strain gauge and the weld toe. Fig. 10 shows two examples specimens set-up with 1.5mm grid length strain gauge, specifically the Test-1 and Test-3 specimen of Table 5. Similarly, Fig. 11 shows the Test-4 specimen along with a view on the area where the 0.6mm grid length strain gauges were applied together with a technical drawing to better understand their positioning. All the specimens were tested in as-welded condition.

It should be noted that given the irregular geometry of the weld bead, strain gauges position with respect to the weld toe can be affected by an inherent error in radial direction. In addition, it is expected that strain gauges belonging to different specimens but placed in the same nominal angular and radial coordinate, will produce different experimental read-

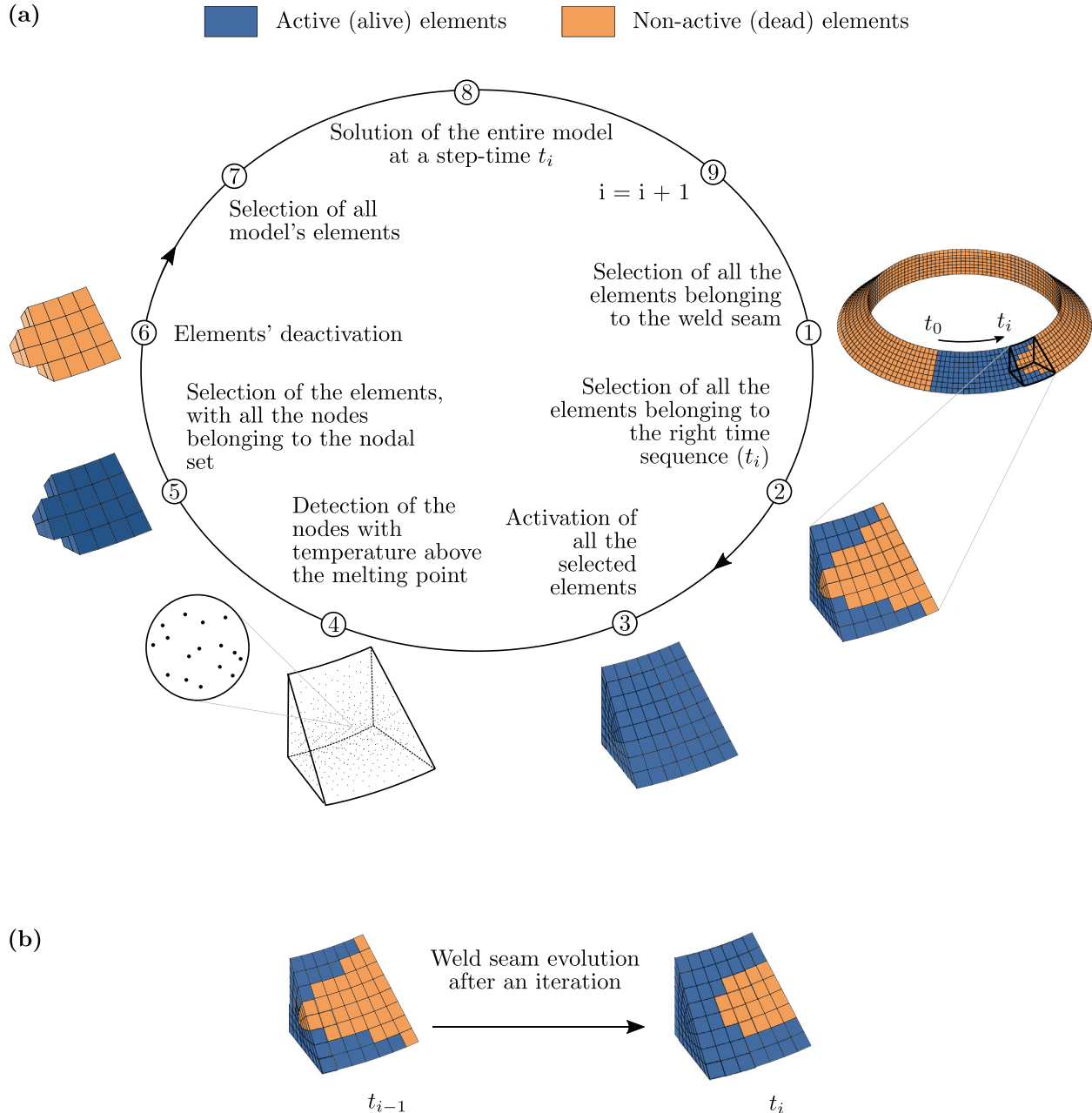


Fig. 9. Graphic representation of the iterative process required to perform the RWP method (a), and example of active and inactive elements evolution in a weld seam section (b)

ings. For these reasons a certain variability in the experimental data is expected and it will be treated through a standard deviation estimated on the basis of the different performed measurements.

With reference to Fig. 11a, the run in-run out point is identified by the location where the welding torch begins and ends the process. It is worth noting that the material under these circumstances is affected by a double thermal process, whereby residual stress and strain values can significantly deviate from an axisymmetric condition.

As described in Section 2, the stress relaxation was performed by a progressive material removal from the back surface of the plate. Through material removal, relaxed strains have been progressively measured as a function of the radial distance (Δr_{ext}), angular coordinate (θ), incremental hole depth coordinate (δ) and hole diameter (d), as summarized in Eq. 4

$$\varepsilon_{rr} = f(r, \theta, \delta, d) \quad (4)$$

As reported in Tables 6 and 7, several measurements have been gathered from a single strain gauge, by maintaining Δr_{ext} and θ fixed and varying δ and d . For ease of comprehension, only the data obtained during the 100mm hole are reported since the readings obtained during the 42mm hole fall within the background noise. Table 6 summarizes relaxed radial strain measured through 1.5mm grid length strain gauges, while Table 7 summarizes relaxed radial strain measured through 0.6mm grid length strain gauges. In either cases, results have been reported as function of the strain gauge position (i.e. angular coordinate θ and radial distance Δr_{ext}) and the hole cutting depth δ . Since the drilling was done by incremental steps of 5mm, δ gets discrete values of 5mm, 10mm, 15mm and 20mm.

As can be noticed from both Tables 6 and 7, an higher number of strain gauge readings were obtained in the vicinity of the weld toe (i.e. $\Delta r_{ext} = 6.5\text{mm}$), since residual radial stresses increase approaching the

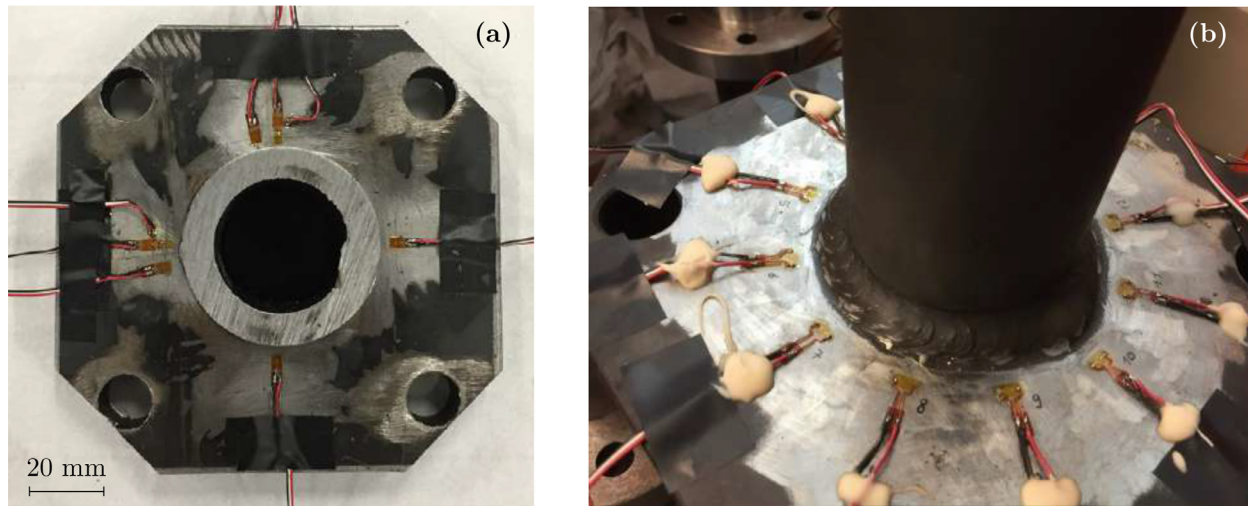


Fig. 10. *Test-1* specimen, with eight strain gauges applied at a 90° step angle (a); *Test-3* specimen with twelve applied strain gages with 30° step angles (b)

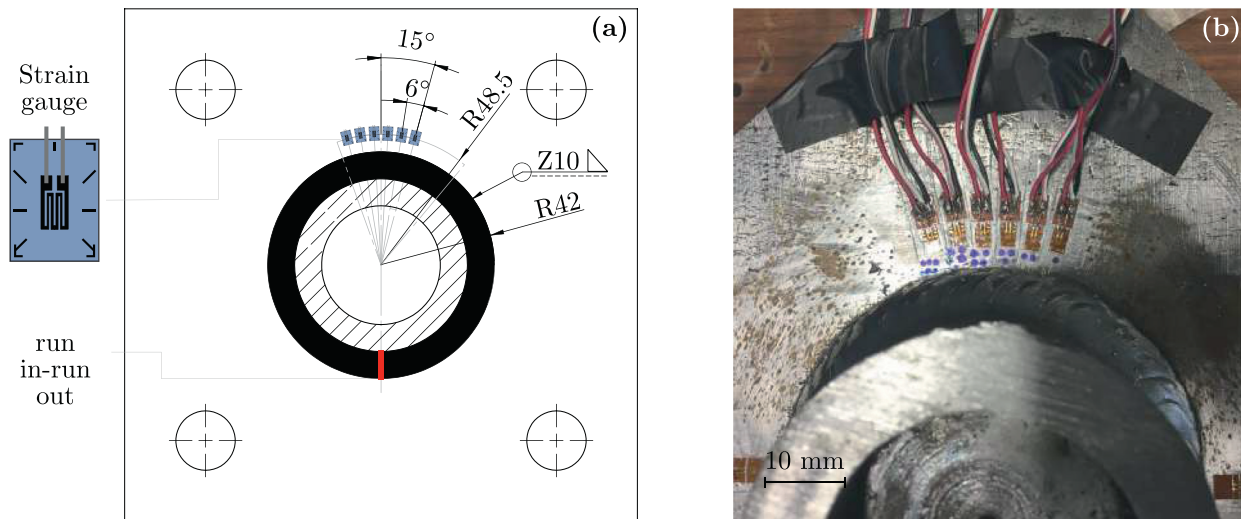


Fig. 11. Technical drawing of the strain gauges positioning over a small arc of circumference (a), picture of the actual bead geometry at the point of application of the 0.6mm grid length strain gauges (b)

weld toe in radial direction. However, due to the steep gradient, the result variability obtained from the uneven weld bead geometry increases getting closer to the weld notch. For this reason, it is advisable not to rely on a single strain gauge reading and consider the variability in the results provided by more data, instead. This approach is adopted in the following [Section 5](#), where experimental and numerical results have been compared with regards to their mean values and standard deviations.

5. Results and discussion

In this section numerical and experimental measurements of relaxed radial strains (ϵ_{Rrr}) are presented, together with a data analysis and discussion. Firstly, the experimental results of ϵ_{Rrr} as a function of θ are presented in [Section 5.1](#). Secondly, the experimental results of ϵ_{Rrr} as a function of θ , related to the 0.6mm grid length strain gauges are given in [Section 5.2](#), with the aim of achieving additional indication about measurements variability related to the weld toe irregularities. In [Section 5.3](#), numerical and experimental results of relaxed radial strain are compared to obtain an overall validation of the numerical model. Finally, in the following [Section 6](#) numerical residual stresses are discussed, specifically for the plate surface region close to the weld bead, where the fatigue crack can originate.

5.1. Experimental results of relaxed radial strain

Experimental results of relaxed radial strain (ϵ_{Rrr}) as a function of the hoop coordinate (θ) are shown in [Fig. 12](#) for a fixed strain gauge radial distance of $\Delta r_{ext} = 6.5\text{mm}$. In the figure two macro-regions can be roughly identified: group A, influence area of the run in-run out region and group B region where strain results can be assumed quasi axisymmetric. It should be noted that data trend is significantly different between the two macro-regions; this is why the study of the two regions has been separated in order to enable a more accurate analysis of both numerical and experimental results.

The first region (i.e. group A), included in an approximate angular domain⁴ $\theta \in [-60^\circ, 60^\circ]$, is affected by a double thermal process due to the beginning and end of the welding process and therefore presents a considerable results variation. On the contrary, in the second region (i.e. group B), included in the approximate angular domain $\theta \in (60^\circ, 300^\circ)$, a quasi-constant ϵ_{Rrr} along θ can be observed. Data belonging to group A present mean values of 1.80×10^{-5} and 3.17×10^{-5} , and standard deviations of 1.10×10^{-4} and 1.66×10^{-4} for $\delta = 10\text{mm}$ and $\delta = 15\text{mm}$ respectively.

⁴ The range and domain are intended as mathematical concepts

Table 6

Summary of experimental relaxed strains measurements in **bold** ($\mu\epsilon$) for 1.5mm grid length strain gauges and hole diameter $d = 100mm$

Test-1				Test-2							
$\theta(^{\circ})$	$\Delta r_{ext}(mm)$	$\delta(mm)$		$\theta(^{\circ})$	$\Delta r_{ext}(mm)$	$\delta(mm)$					
		5	10	15	20	5	10				
0	6.5	/	281	652	3299	0	9				
0	13	/	298	482	408	90	6.5				
5	6.5	/	460	577	1114	90	13				
90	9	/	233	440	2143	180	6.5				
180	9	/	297	600	836	180	13				
270	6.5	/	236	337	1360	270	9				
270	13	/	294	274	270						
275	6.5	/	248	307	760						
Test-3											
$\theta(^{\circ})$	$\Delta r_{ext}(mm)$	$\delta(mm)$			$\theta(^{\circ})$	$\Delta r_{ext}(mm)$	$\delta(mm)$				
		5	10	15	20		5	10	15	20	
0	6.5	28	165	329	1556	15	6.5	148	222	400	2137
30	6.5	65	184	332	1720	30	6.5	87	132	251	1884
60	6.5	0	135	204	770	45	6.5	53	94	181	1693
90	6.5	4	163	255	972	60	6.5	26	124	221	1659
120	6.5	12	148	224	1090	75	6.5	14	93	202	1668
150	6.5	19	144	245	1496	90	6.5	9	99	202	1673
180	6.5	13	145	285	1926						
210	6.5	15	142	309	2281						
240	6.5	7	113	262	2170						
270	6.5	-3	109	260	2090						
300	6.5	-17	96	190	1997						
330	6.5	-32	85	149	564						

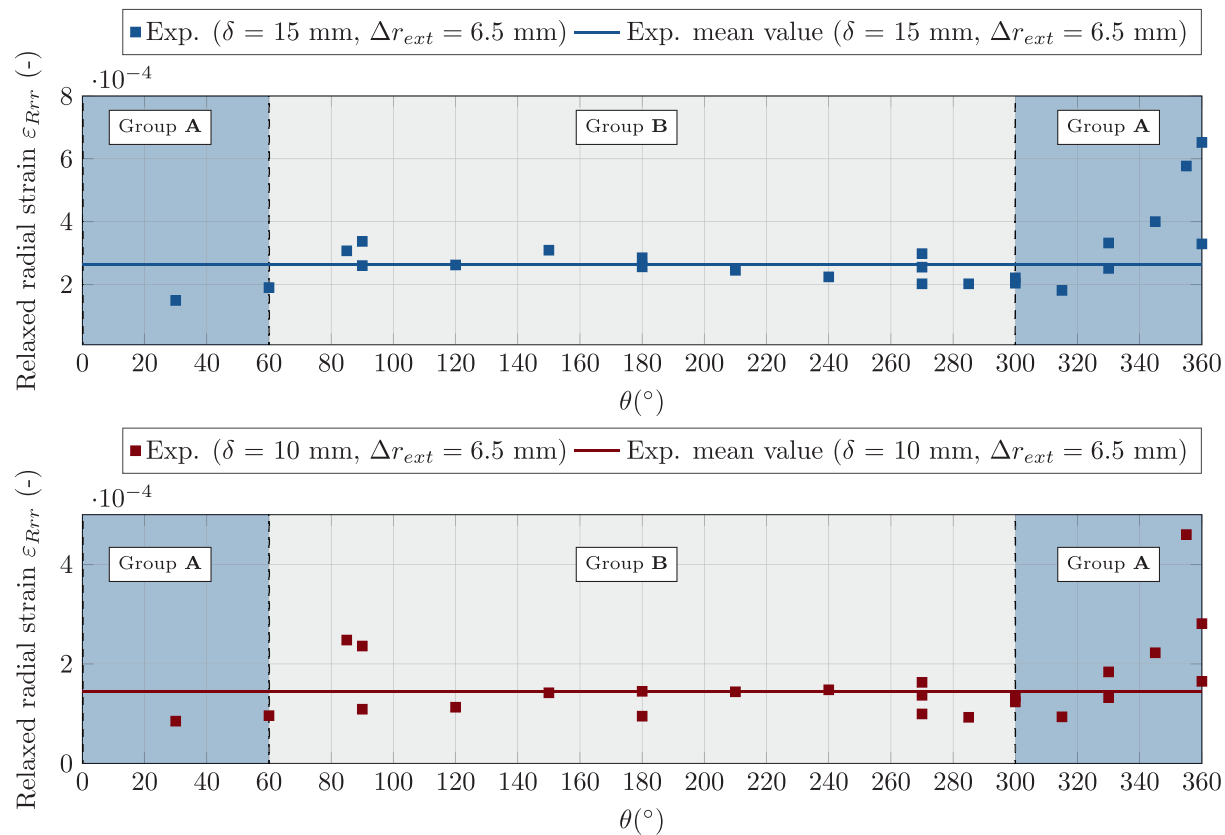


Fig. 12. Relaxed radial strain over specimen hoop coordinate measured through 1.5mm grid length strain gauges for a fixed strain gauge radial distance of $\Delta r_{ext} = 6.5mm$. The mean value line was obtained considering only group B measurements

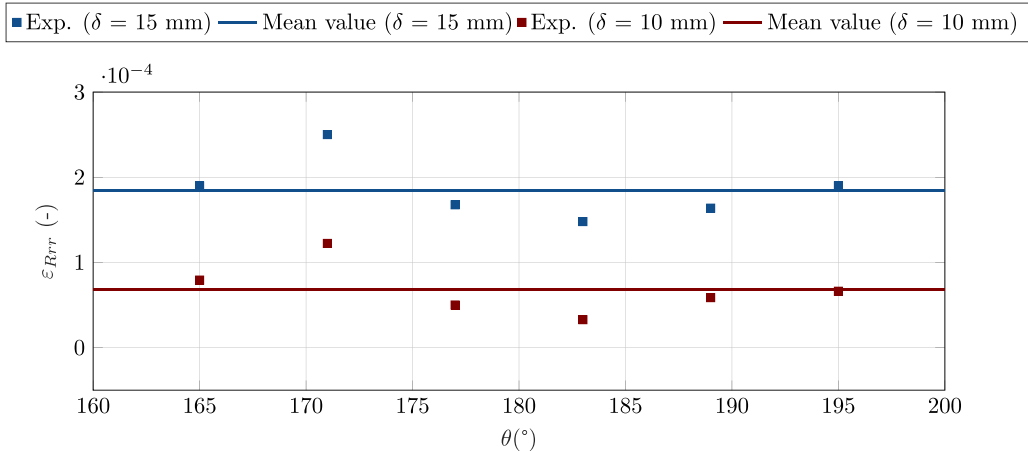


Fig. 13. Relaxed radial strain data over the hoop coordinate measured through 0.6mm grid length strain gauges; mean values are plotted as continuous lines

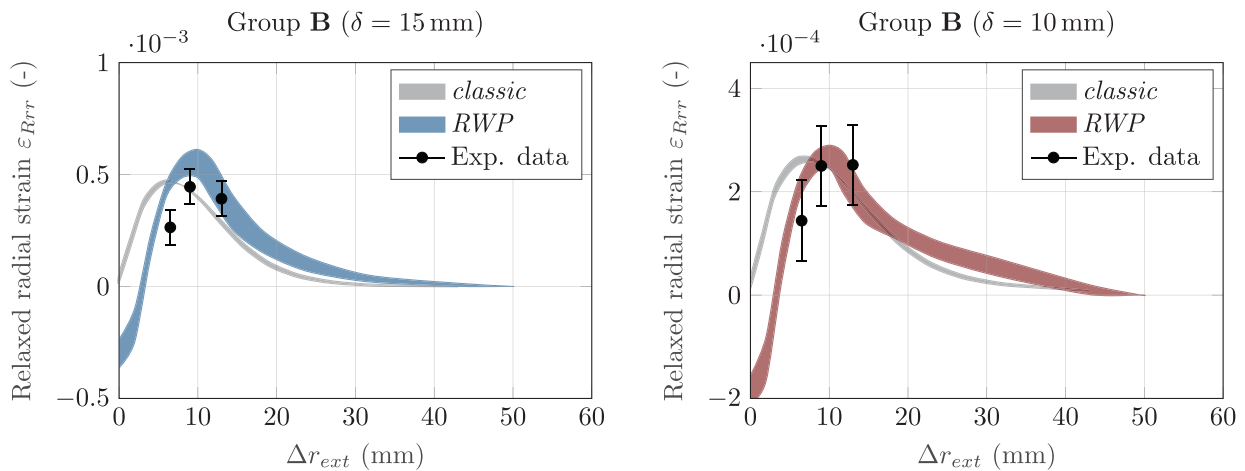


Fig. 14. Comparison between numerical and experimental data of relaxed radial strains over distance from the weld toe for two different incremental hole depths in the group B. Experimental results are presented through mean value and standard deviation while numerical results are the convex hull of ε_{Rrr} data obtained in the angular domain $\theta \in (60^\circ, 300^\circ)$

Table 7
Summary of experimental relaxed strains measurements in **bold** ($\mu\epsilon$) for 0.6mm grid length strain gauges and hole diameter $d = 100\text{mm}$

Test-4		$\delta(\text{mm})$			
θ°	$\Delta r_{ext}(\text{mm})$	5	10	15	20
195	6.5	51	66	190	1983
189	6.5	20	59	164	1987
183	6.5	9	33	148	1929
177	6.5	36	50	168	1919
171	6.5	78	122	250	1912
165	6.5	27	79	190	1889

tively. Data belonging to group B present mean values of 1.44×10^{-4} and 2.64×10^{-5} , and standard deviations of 4.9×10^{-5} and 4.1×10^{-5} for $\delta = 10\text{mm}$ and $\delta = 15\text{mm}$ respectively.

Due to intrinsic stress variability in group A, it should be difficult to obtain a sound standard deviation value by considering all data as a single group. For this reason, a process-related variability regarding experimental relaxed strain measurements has been defined by averaging standard deviations of Group B data for $\delta = 10\text{mm}$ and $\delta = 15\text{mm}$. The data involved refer to all categories of strain gauges used, i.e. 0.6mm

and 1.5mm grid length strain gauges, obtaining a process-related standard deviation equal to 7.8×10^{-5} .

5.2. Strain sensitivity to dimensional variation of the weld seam geometry

It is reasonable to expect that relaxed strains are affected by different sources of error, such as those related to accurate positioning of the grid or variability of the local weld geometry.

As already shown in Fig. 12, relaxed radial strain has an almost constant trend in the angular domain $\theta \in (60^\circ, 300^\circ)$; for this reason, a group of strain gauges were placed between 165° and 195° , spaced by an angle of 6° , to better achieve indication of the intrinsic variation due to the uneven geometry of the weld toe. Strain gauges with a grid length of 0.6mm were employed to obtain measurements shown in Table 7.

Fig. 11 shows a technical drawing of the strain gauges placement together with a picture of the actual specimen geometry. As can be seen from Fig. 11b, the bead geometry is not as ideal as the one implemented within the finite element model, this leads to a variable strain distribution at points where it is supposed to be constant. Fig. 13 shows experimental results acquired from the measurements described above. It can be noticed that the ε_{Rrr} trend vs the angular coordinate is almost constant, for different δ coordinates. A standard deviation of 3.0×10^{-5} and 3.5×10^{-5} and mean values of 6.8×10^{-4} and 1.84×10^{-4} have been calculated respectively for $\delta = 10\text{mm}$ and $\delta = 15\text{mm}$. It is supposed that the observed variability mainly comes from the weld irregularities. The cal-

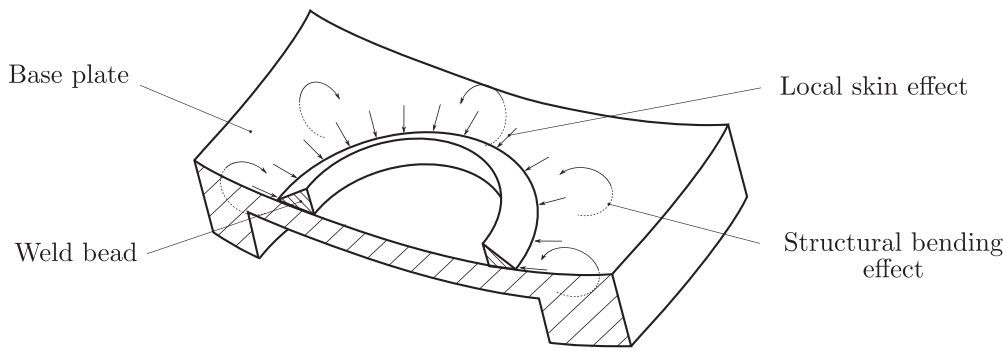


Fig. 15. Cross-sectional view of the base plate and weld bead with outlined the bending and skin effects due to the incremental cutting process

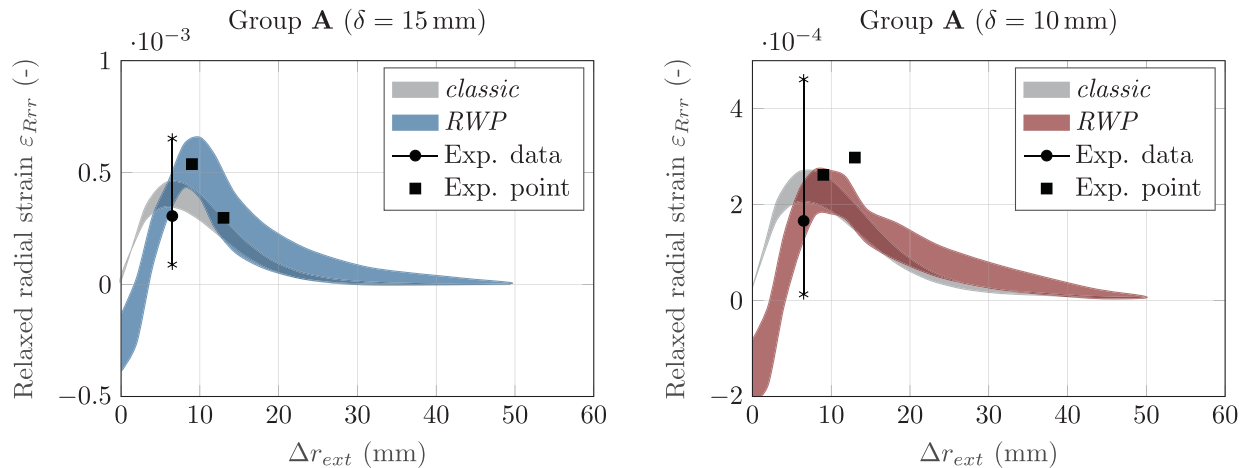


Fig. 16. Comparison between numerical and experimental data of relaxed radial strains over distance from the weld toe for two different incremental hole depths in the group A. Experimental results are reported through of mean value and standard deviation while numerical results are the convex hull of ε_{Rrr} data obtained for two angular domains $\theta \in [-60^\circ, 60^\circ]$

culated standard deviations are comparable to the ones obtained from 1.5mm grid length strain gauges of Fig. 12, which is an independent verification of the experimental reading reliability.

5.3. Comparison between experimental and numerical relaxed strain

Since it has been already observed that relaxed strain results differ greatly between the two macro-regions (i.e. group A and group B), it was considered appropriate to study in detail these two regions, separately, according to the radial distance Δr_{ext} .

Fig. 14 shows a comparison between ε_{Rrr} results for the *classic* and *RWP* methods as a function of Δr_{ext} for two incremental hole depths $\delta = 10 \text{ mm}$ and $\delta = 15 \text{ mm}$ in the angular domain $\theta \in (60^\circ, 300^\circ)$. Numerical results are presented as the convex hull of ε_{Rrr} over Δr_{ext} in the angular range considered (which is equivalent not to consider the dependence on the angular coordinate), while experimental measurements are reported through their mean value and standard deviation. Even if measures were taken at three different distances from the weld, the standard deviation obtained for $\Delta r_{ext} = 6.5 \text{ mm}$ was applied to all measurements. This was suggested by the fact that more data were available for $\Delta r_{ext} = 6.5 \text{ mm}$; moreover this was considered to be conservative, in the sense that a lower variability is expected for larger distances from the weld.

Regarding the comparison between numerical methods, both *classic* and *RWP* methods show a similar behavior for $\Delta r_{ext} > 13 \text{ mm}$; however, a significant difference can be noticed in the surrounding area of the weld toe. In this case, the *RWP* method yields compressive (negative) strains for $\Delta r_{ext} = 0$, while the *classic* method always predicts positive relaxed radial strains. In addition, for the *classic* method, the gradient of ε_{Rrr} close to the weld toe turns out to be lower with respect the *RWP*

method. These aspects, in fact, is what mainly differentiates the two models and brings the *RWP* closer to experimental data.

Although the difference between numerical and experimental results can appear considerable, it must be remembered that several assumptions have been done within the thermal-structural numerical model and experimental data examined above, the most relevant being listed below:

- simplified specimen geometry, specifically, weld seam irregularities were not considered in the FE-model;
- temperature-dependant elastic-plastic material properties largely varies within the same material between different literature sources;
- temperature field was described by a simplified thermal model (CIT);
- possibility of strain gauge positioning errors, both in the radial and angular direction;
- strain gauge readings represent an averaged over the reading grid.

It is worth noting that the unusual relaxed radial strain behavior showed in Fig. 14 can be clarified by introducing two structural effects related to the incremental cutting process. If, in an approximate way, the thermal induced shrinking of the the seam weld is considered, a structural bending and a local skin effect arise, both exemplified in the cross-sectional view of Fig. 15. The progressive cutting, starting from the lower plate surface, allows the upper part to bend due to stress relieving. At the same time, weld bead contraction generates a skin-positive radial effect. During incremental drilling these two factors will combine generating the strain profile of Fig. 14.

For the sake of clarity, group A results are also presented in Fig. 16. In this case, as already mentioned, given the trend of experimental data the calculation of a standard deviation seems unwise. For this reason, the total ε_{Rrr} range has been reported (i.e. represented by asterisks) with

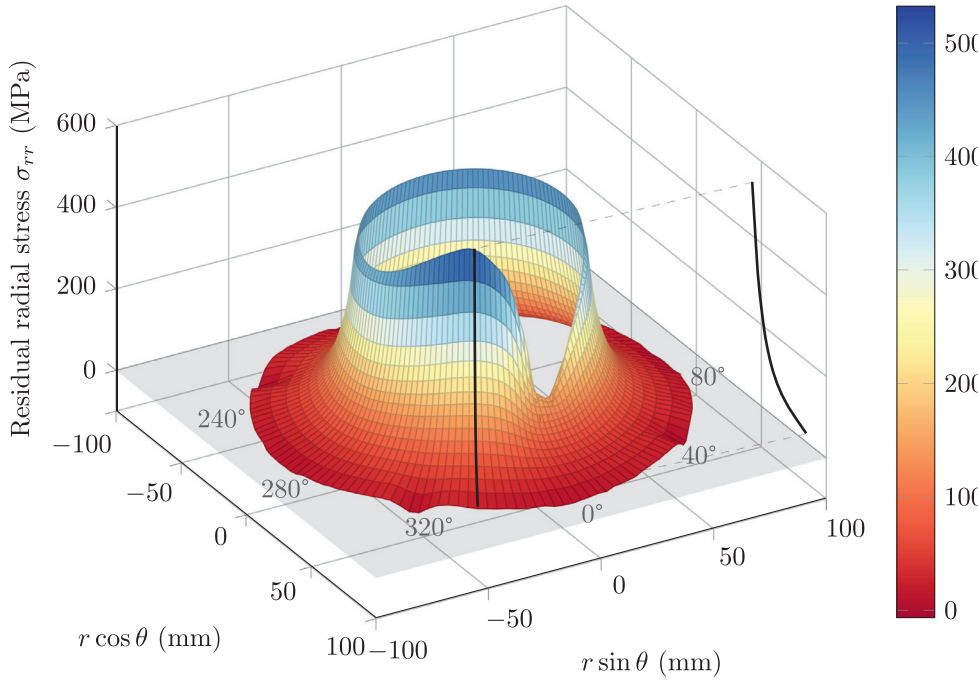


Fig. 17. Overall residual radial stress field on the plate surface ($z = 0$), for a radial domain $r \in [42\text{mm}, 78\text{mm}]$

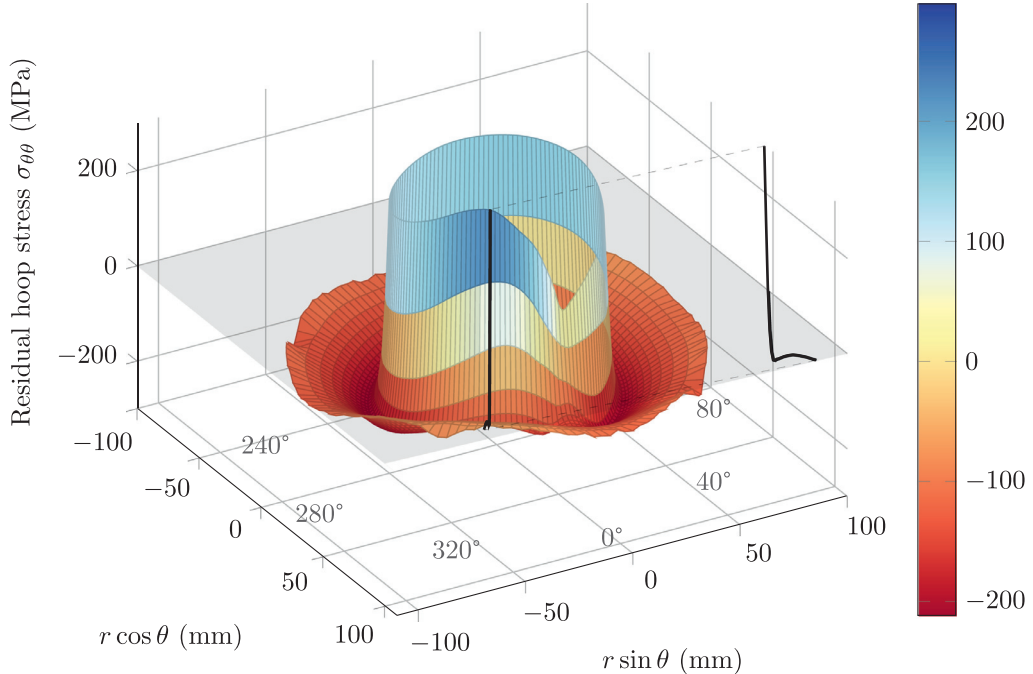


Fig. 18. Overall residual hoop stress field on the plate surface ($z = 0$), for a radial domain of $r \in [42\text{mm}, 78\text{mm}]$

the mean value also indicated. The lack of data for $\Delta r_{ext} = 9\text{mm}$ and $\Delta r_{ext} = 13\text{mm}$ does not allow the identification of a mean value, making the use of the standard deviation unnecessary as well. Therefore, for $\Delta r_{ext} = 9\text{mm}$ and $\Delta r_{ext} = 13\text{mm}$, the experimental points available have been directly reported.

With the exception of the experimental point at $\Delta r_{ext} = 13\text{mm}$ and $\delta = 10\text{mm}$, numerical results relative to the RWP method were well predicted from experimental data. With regard to the comparison between the numerical methods, the observations made earlier regarding Fig. 14 remain unchanged. For instance both methods resemble each other in the descending ϵ_{Rrr} phase while they behaved quite differently in the proximity of the weld toe.

6. Residual stresses due to the welding process

This section presents numerical data of residual hoop and radial stress, in order to investigate their behavior and assess the numerical model accuracy. Fig. 17 shows the global residual radial stress field on the plate surface, around the weld seam. The figure displays radial stresses in the radial domain $r \in [42\text{mm}, 78\text{mm}]$ on the upper plate surface. Similarly, Fig. 18 shows the hoop stress around the weld bead in the same radial domain $r \in [42\text{mm}, 78\text{mm}]$. It can be observed that both figures clearly identify the run in-run out point through the angular coordinate at $\theta = 0^\circ$. For the sake of clarity, the 2D-curve of maximum stress is also represented (i.e. black line), as a projection on the vertical

plane, as well as the $z = 0\text{mm}$ plane (i.e. light grey plane). Because of the notch effect given by the weld seam, the maximum stress is globally reached in the weld toe both for radial and hoop residual stresses. Especially for residual radial stress, the maximum stress value reached is 507MPa which exceeds the yield strength of the material at room temperature. It is interesting to notice that radial stresses increment was found in a region quite close to the weld toe; referring to Fig. 17, in about $\approx 7\text{mm}$ distance from the weld toe, radial stress increases from $\approx 150\text{MPa}$ to $\approx 500\text{MPa}$. The residual stress may rise beyond the yield point in localized areas, due to the high stress concentrations [59]. It has to be considered that the weld toe had been shaped with null radius, resulting in a high stress/strain gradient near the notch. However, relaxed radial strains were obtained sufficiently far away, in area where the highest gradient had probably no effect.

In the case of radial residual stress the maximum stress value is reached for an angle of 331° , while in the case of hoop residual stress the maximum is reached for an angle of 324° . It is worth noting that in both cases the stress surface is axisymmetric for θ values far from the run in-run out point. Actually, for $\theta = 0^\circ$ there is a significant stress reduction both in radial and hoop stresses of 270MPa and 210MPa respectively; similar results have been experienced in a tube-tube welded joint when residual stresses were evaluated through the hole drilling technique by Sepe et al. [60].

Residual radial stresses are always positive, showing a monotonous growing behavior for $\Delta r_{ext} \rightarrow 0$. On the contrary, residual hoop stresses are mostly compressive, except for a region close to the weld toe, where the stress gradient is steeper compare residual radial stresses.

For clarity of interpretation, Figs. 17 and 18 show ripples in the stress surface for stress values close to zero. This unusual behavior is due to the quadrangular geometry of the plate and the presence of four holes on the plate corners. This behavior, however, is related to a surface region of low stress gradient and presents a negligible stress variation compared to the stress gradient in the weld toe area.

7. Conclusions

In the present work numerical and experimental data of relaxed strains and residual stresses have been presented and discussed for a welded pipe-to-plate joint. The obtained results seems significant for the field, since residual stresses are considered to have a detrimental effect on the fatigue strength. The research activity carried out and the obtained results allow to draw the following conclusions:

- the thermal model employed (CIT) is straightforward to be implemented and requires only one setting parameter; although its simplicity, once calibrated, it can provide fairly good results both from a thermal and structural point of view;
- in order not to overestimate residual stresses, the implementation of temperature dependent elastic-plastic material properties is recommended during the simulation of a weld seam deposition process, since weld roots and toes can act as sharp notches ;
- three-dimensional modeling of the welding process is necessary to accurately capture variations in the stress/strain field along the circumferential direction;
- the *representative welding process* showed a better agreement with experimental results, if compared to the *classic* method; this can be attributed to a more accurate description of the actual weld seam stiffness during the cooling process;
- the use of a uncoupled numerical simulation, wherever possible, allows to have great flexibility on both the implemented thermal and structural models, leading to a very flexible simulation of the welding process;
- relaxed strains measures are intrinsically affected by experimental errors; a reproduction of the experimental readings between different samples seems to be a difficult task; it is therefore necessary to

deal with a degree of uncertainty during the incremental cutting experimental phase;

- the run in-run out point exhibits a significant stress reduction in the weld toe, most likely as a result of the double thermal process that this area undergoes;
- the obtained results give a deep insight of the residual stress distribution nearby the weld for the examined specimen and will be used for subsequent fatigue assessment.

Declaration of Competing Interest

The authors declare that they have no known competing financial interests or personal relationships that could have appeared to influence the work reported in this paper.

CRediT authorship contribution statement

Andrea Chiocca: Conceptualization, Formal analysis, Software, Methodology, Writing - original draft. **Francesco Frendo:** Data curation, Supervision, Formal analysis, Writing - review & editing. **Leonardo Bertini:** Data curation, Supervision, Formal analysis, Writing - review & editing.

References

- [1] Clarin M. High strength steel local buckling and residual stresses. Department of Civil and Environmental Engineering. Lulea, Lulea University of Technology. Licentiate, 2004.
- [2] Barsoum Z, Barsoum I. Residual stress effects on fatigue life of welded structures using LEFM. Eng. Fail. Anal. 2009;16(1):449–67. doi:[10.1016/j.engfailanal.2008.06.017](https://doi.org/10.1016/j.engfailanal.2008.06.017).
- [3] Vanboven G, Chen W, Rogge R. The role of residual stress in neutral pH stress corrosion cracking of pipeline steels. part i: pitting and cracking occurrence. Acta Mater. 2007;55(1):29–42. doi:[10.1016/j.actamat.2006.08.037](https://doi.org/10.1016/j.actamat.2006.08.037).
- [4] Bartolozzi R, Frendo F. Stiffness and strength aspects in the design of automotive coil springs for McPherson front suspensions: a case study. Proceed. Inst. Mech. Eng. Part D 2011;225(10):1377–91. doi:[10.1177/0954407011403853](https://doi.org/10.1177/0954407011403853).
- [5] Montanari R, Fava A, Barbieri G. Experimental techniques to investigate residual stress in joints. Residual Stress Analysis on Welded Joints by Means of Numerical Simulation and Experiments. InTech; 2018. doi:[10.5772/intechopen.71564](https://doi.org/10.5772/intechopen.71564).
- [6] Zheng B, Yang S, Jin X, Shu G, Dong S, Jiang Q. Test on residual stress distribution of welded s600e high-strength stainless steel sections. J. Constr. Steel Res. 2020;168:105994. doi:[10.1016/j.jcsr.2020.105994](https://doi.org/10.1016/j.jcsr.2020.105994).
- [7] Zarandi EP, Skallerud BH. Experimental and numerical study of mooring chain residual stresses and implications for fatigue life. Int. J. Fatigue 2020;135:105530. doi:[10.1016/j.ijfatigue.2020.105530](https://doi.org/10.1016/j.ijfatigue.2020.105530).
- [8] Goel S, Neikter M, Capek J, Polatidis E, Colliander MH, Joshi S, et al. Residual stress determination by neutron diffraction in powder bed fusion-built alloy 718: Influence of process parameters and post-treatment. Mater. Des. 2020;195:109045. doi:[10.1016/j.matdes.2020.109045](https://doi.org/10.1016/j.matdes.2020.109045).
- [9] Joshi S, Walton JR. Reconstruction of the residual stresses in a hyperelastic body using ultrasound techniques. Int. J. Eng. Sci. 2013;70:46–72. doi:[10.1016/j.ijengsci.2013.05.001](https://doi.org/10.1016/j.ijengsci.2013.05.001).
- [10] Xu C, Song W, Pan Q, Li H, Liu S. Nondestructive testing residual stress using ultrasonic critical refracted longitudinal wave. Phys. Procedia 2015;70:594–8. doi:[10.1016/j.phpro.2015.08.030](https://doi.org/10.1016/j.phpro.2015.08.030).
- [11] Alpsten GA. Thermal residual stresses in hot-rolled steel members, december 1968. Tech. Rep., Fritz Laboratory Reports; 1968.
- [12] Nitschke-Pagel TN. Limitations and recommendations for the measurement of residual stresses in welded joints. In: Residual Stresses 2018, vol. 6. Materials Research Proceedings; 2018. p. 221–6. doi:[10.21741/9781945291890-35](https://doi.org/10.21741/9781945291890-35).
- [13] Ridgeway CD, Gu C, Ripplinger K, Detwiler D, Ji M, Soghrati S, et al. Prediction of location specific mechanical properties of aluminum casting using a new CA-FEA (cellular automaton-finite element analysis) approach. Mater. Des. 2020;194:108929. doi:[10.1016/j.matdes.2020.108929](https://doi.org/10.1016/j.matdes.2020.108929).
- [14] Gref T, Nardi VG, Schmid S, Hoyer J, Rizaiy Y, Boll T, et al. Vertical continuous compound casting of copper aluminum bilayer rods. J. Mater. Process. Technol. 2021;288:116854. doi:[10.1016/j.jmatprotec.2020.116854](https://doi.org/10.1016/j.jmatprotec.2020.116854).
- [15] Anglada E, Meléndez A, Obregón A, Villanueva E, Garmendia In. Performance of optimization algorithms in the model fitting of the multi-scale numerical simulation of ductile iron solidification. Metals 2020;10(8):1071. doi:[10.3390/met10081071](https://doi.org/10.3390/met10081071).

- [16] Jayakrishna P, Chakraborty S, Ganguly S, Talukdar P. A novel method for determining the three dimensional variation of non-linear thermal resistance at the mold-strand interface in billet continuous casting process. *Int. Commun. Heat Mass Transf.* 2020;119:104984. doi:[10.1016/j.icheatmasstransfer.2020.104984](https://doi.org/10.1016/j.icheatmasstransfer.2020.104984).
- [17] Sandeep M, Sandeep M. Modeling and analysis of residual stresses in castings using AlSi12(fe) and NiCu30(fe) materials. *IOP Confer. Ser.* 2020;912:032047. doi:[10.1088/1757-899x/912/3/032047](https://doi.org/10.1088/1757-899x/912/3/032047).
- [18] Bhatti AA, Barsoum Z, Murakawa H, Barsoum I. Influence of thermo-mechanical material properties of different steel grades on welding residual stresses and angular distortion. *Mater. Des.* (1980-2015) 2015;65:878-89. doi:[10.1016/j.matdes.2014.10.019](https://doi.org/10.1016/j.matdes.2014.10.019).
- [19] Capriccioni A, Frosi P. Multipurpose ANSYS FE procedure for welding processes simulation. *Fusion Eng. Des.* 2009;84(2-6):546-53. doi:[10.1016/j.fusengdes.2009.01.039](https://doi.org/10.1016/j.fusengdes.2009.01.039).
- [20] Xin H, Veljkovic M. Residual stress effects on fatigue crack growth rate of mild steel s355 exposed to air and seawater environments. *Mater. Des.* 2020;193:108732. doi:[10.1016/j.matdes.2020.108732](https://doi.org/10.1016/j.matdes.2020.108732).
- [21] Chen J, Salvati E, Uzun F, Papadaki C, Wang Z, Everaerts J, et al. An experimental and numerical analysis of residual stresses in a TIG weldment of a single crystal nickel-base superalloy. *J. Manuf. Process.* 2020;53:190-200. doi:[10.1016/j.jmapro.2020.02.007](https://doi.org/10.1016/j.jmapro.2020.02.007).
- [22] Hemmesi K, Farajian M, Boin M. Numerical studies of welding residual stresses in tubular joints and experimental validations by means of x-ray and neutron diffraction analysis. *Mater. Des.* 2017;126:339-50. doi:[10.1016/j.matdes.2017.03.088](https://doi.org/10.1016/j.matdes.2017.03.088).
- [23] Hemmesi K, Mallet P, Farajian M. Numerical evaluation of surface welding residual stress behavior under multiaxial mechanical loading and experimental validations. *Int. J. Mech. Sci.* 2020;168:105127. doi:[10.1016/j.ijmecsci.2019.105127](https://doi.org/10.1016/j.ijmecsci.2019.105127).
- [24] Lee J-H, Jang B-S, Kim H-J, Shim SH, Im SW. The effect of weld residual stress on fracture toughness at the intersection of two welding lines of offshore tubular structure. *Mar. Struct.* 2020;71:102708. doi:[10.1016/j.marstruc.2020.102708](https://doi.org/10.1016/j.marstruc.2020.102708).
- [25] Asadi P, Alimohammadi S, Kohantobri O, Fazli A, Akbari M. Effects of material type, preheating and weld pass number on residual stress of welded steel pipes by multi-pass TIG welding (c-mn, SUS304, SUS316). *Therm. Sci. Eng. Prog.* 2020;16:100462. doi:[10.1016/j.tsep.2019.100462](https://doi.org/10.1016/j.tsep.2019.100462).
- [26] Lin J, Ma N, Liu X, Lei Y. Modification of residual stress distribution in welded joint of titanium alloy with multi electron beam heating. *J. Mater. Process. Technol.* 2020;278:116504. doi:[10.1016/j.jmatprotec.2019.116504](https://doi.org/10.1016/j.jmatprotec.2019.116504).
- [27] Ansaripour N, Heidari A, Eftekhari SA. Multi-objective optimization of residual stresses and distortion in submerged arc welding process using genetic algorithm and harmony search. *Proced. Instit. Mech. Eng. Part C* 2019;234(4):862-71. doi:[10.1177/0954406219885977](https://doi.org/10.1177/0954406219885977).
- [28] Majidi HR, Torabi AR, Zabihli M, Razavi SMJ, Berto F. Energy-based ductile failure predictions in cracked friction-stir welded joints. *Eng. Fail. Analy.* 2019;102:327-37. doi:[10.1016/j.englfailanal.2019.04.066](https://doi.org/10.1016/j.englfailanal.2019.04.066).
- [29] Lu Y, Zhu S, Zhao Z, Chen T, Zeng J. Numerical simulation of residual stresses in aluminum alloy welded joints. *J. Manuf. Process.* 2020;50:380-93. doi:[10.1016/j.jmapro.2019.12.056](https://doi.org/10.1016/j.jmapro.2019.12.056).
- [30] Xiao Z, Chen C, Zhu H, Hu Z, Nagarajan B, Guo L, et al. Study of residual stress in selective laser melting of ti6al4v. *Mater. Des.* 2020;193:108846. doi:[10.1016/j.matdes.2020.108846](https://doi.org/10.1016/j.matdes.2020.108846).
- [31] Song X, Feih S, Zhai W, Sun C-N, Li F, Maiti R, et al. Advances in additive manufacturing process simulation: Residual stresses and distortion predictions in complex metallic components. *Mater. Des.* 2020;193:108779. doi:[10.1016/j.matdes.2020.108779](https://doi.org/10.1016/j.matdes.2020.108779).
- [32] Wagener R, Hell M, Scurria M, Bein T. Deriving the structural fatigue behavior of additively manufactured components. In: *TMS 2020 149th Annual Meeting & Exhibition Supplemental Proceedings*. Springer International Publishing; 2020. p. 139-49. doi:[10.1007/978-3-030-36296-6_13](https://doi.org/10.1007/978-3-030-36296-6_13).
- [33] Razavi SMJ, Hooreweder BV, Berto F. Effect of build thickness and geometry on quasi-static and fatigue behavior of ti-6al-4v produced by electron beam melting. *Add. Manuf.* 2020;36:101426. doi:[10.1016/j.addma.2020.101426](https://doi.org/10.1016/j.addma.2020.101426).
- [34] Schnabel K, Baumgartner J, Mller B. Fatigue assessment of additively manufactured metallic structures using local approaches based on finite-element simulations. *Procedia Struct. Integr.* 2019;19:442-51. doi:[10.1016/j.prostr.2019.12.048](https://doi.org/10.1016/j.prostr.2019.12.048).
- [35] An K, Yuan L, Dial L, Spinelli I, Stoica AD, Gao Y. Neutron residual stress measurement and numerical modeling in a curved thin-walled structure by laser powder bed fusion additive manufacturing. *Mater. Des.* 2017;135:122-32. doi:[10.1016/j.matdes.2017.09.018](https://doi.org/10.1016/j.matdes.2017.09.018).
- [36] Ferro P, Berto F, James NM. Asymptotic residual stress distribution induced by multipass welding processes. *Int. J. Fatigue* 2017;101:421-9. doi:[10.1016/j.ijfatigue.2016.11.022](https://doi.org/10.1016/j.ijfatigue.2016.11.022).
- [37] Zhou Y, Chen XD, Fan ZC, Rao SX. Finite element modelling of welding residual stress and its influence on creep behavior of a 2.25cr-1mo-0.25v steel cylinder. *Procedia Eng.* 2015;130:552-9. doi:[10.1016/j.proeng.2015.12.264](https://doi.org/10.1016/j.proeng.2015.12.264).
- [38] Wang X, Meng Q, Hu W. Numerical analysis of low cycle fatigue for welded joints considering welding residual stress and plastic damage under combined bending and local compressive loads. *Fatigue Fract. Eng. Mater. Struct.* 2020. doi:[10.1111/ffe.13216](https://doi.org/10.1111/ffe.13216).
- [39] Bertini L, Bucchi F, Frendo F, Moda M, Monelli BD. Residual stress prediction in selective laser melting. *Int. J. Adv. Manuf. Technol.* 2019;105(1-4):609-36. doi:[10.1007/s00170-019-04091-5](https://doi.org/10.1007/s00170-019-04091-5).
- [40] Deng D. FEM prediction of welding residual stress and distortion in carbon steel considering phase transformation effects. *Mater. Des.* 2009;30(2):359-66. doi:[10.1016/j.matdes.2008.04.052](https://doi.org/10.1016/j.matdes.2008.04.052).
- [41] Deng D, Murakawa H. Prediction of welding residual stress in multi-pass butt-welded modified 9cr-1mo steel pipe considering phase transformation effects. *Comput. Mater. Sci.* 2006;37(3):209-19. doi:[10.1016/j.commatsci.2005.06.010](https://doi.org/10.1016/j.commatsci.2005.06.010).
- [42] Hu Y-F, Chung K-F, Ban H, Nethercot DA. Investigations into residual stresses in s690 cold-formed circular hollow sections due to transverse bending and longitudinal welding. *Eng. Struct.* 2020;219:110911. doi:[10.1016/j.engstruct.2020.110911](https://doi.org/10.1016/j.engstruct.2020.110911).
- [43] Lei Z, Zou J, Wang D, Guo Z, Bai R, Jiang H, et al. Finite-element inverse analysis of residual stress for laser welding based on a contour method. *Opt. Laser Technol.* 2020;129:106289. doi:[10.1016/j.optlastec.2020.106289](https://doi.org/10.1016/j.optlastec.2020.106289).
- [44] Reda R, Magdy M, Rady M. Ti-6al-4v TIG weld analysis using FEM simulation and experimental characterization. *Iran. J. Sci. Technol. Trans. Mech. Eng.* 2019;44(3):765-82. doi:[10.1007/s40997-019-00287-y](https://doi.org/10.1007/s40997-019-00287-y).
- [45] Chiocca A, Frendo F, Bertini L. Evaluation of heat sources for the simulation of the temperature distribution in gas metal arc welded joints. *Metals* 2019;9(11):1142. doi:[10.3390/met9111142](https://doi.org/10.3390/met9111142).
- [46] Chiocca A, Frendo F, Bertini L. Experimental evaluation of relaxed strains in a pipe-to-plate welded joint by means of incremental cutting process. *Procedia Struct. Integr.* 2020;28:2157-67. doi:[10.1016/j.prostr.2020.11.043](https://doi.org/10.1016/j.prostr.2020.11.043).
- [47] Frendo F, Bertini L. Fatigue resistance of pipe-to-plate welded joint under in-phase and out-of-phase combined bending and torsion. *Int. J. Fatigue* 2015;79:46-53. doi:[10.1016/j.ijfatigue.2015.04.020](https://doi.org/10.1016/j.ijfatigue.2015.04.020).
- [48] Bertini L, Cera A, Frendo F. Experimental investigation of the fatigue resistance of pipe-to-plate welded connections under bending, torsion and mixed mode loading. *Int. J. Fatigue* 2014;68:178-85. doi:[10.1016/j.ijfatigue.2014.05.005](https://doi.org/10.1016/j.ijfatigue.2014.05.005).
- [49] Bertini L, Frendo F, Marulo G. Effects of plate stiffness on the fatigue resistance and failure location of pipe-to-plate welded joints under bending. *Int. J. Fatigue* 2016;90:78-86. doi:[10.1016/j.ijfatigue.2016.04.015](https://doi.org/10.1016/j.ijfatigue.2016.04.015).
- [50] Frendo F, Marulo G, Chiocca A, Bertini L. Fatigue life assessment of welded joints under sequences of bending and torsion loading blocks of different lengths. *Fatigue Fract. Eng. Mater. Struct.* 2020. doi:[10.1111/ffe.13223](https://doi.org/10.1111/ffe.13223).
- [51] Salerno G, Bennett CJ, Sun W, Becker AA. Residual stress analysis and finite element modelling of repair-welded titanium sheets. *Weld. World* 2017;61(6):1211-23. doi:[10.1007/s40194-017-0506-1](https://doi.org/10.1007/s40194-017-0506-1).
- [52] Chiocca A, Frendo F, Bertini L. Evaluation of residual stresses in a tube-to-plate welded joint. *MATEC Web Confer.* 2019;300:19005. doi:[10.1051/matecconf/201930019005](https://doi.org/10.1051/matecconf/201930019005).
- [53] Bayock FN, Kah P, Layus P, Karkhin V. Numerical and experimental investigation of the heat input effect on the mechanical properties and microstructure of dissimilar weld joints of 690-MPa QT and TMCP steel. *Metals* 2019;9(3):355. doi:[10.3390/met9030355](https://doi.org/10.3390/met9030355).
- [54] Goldak J, Chakravarti A, Bibby M. A new finite element model for welding heat sources. *Metall. Trans. B* 1984;15(2):299-305. doi:[10.1007/bf02667333](https://doi.org/10.1007/bf02667333).
- [55] Zhu J, Khurshid M, Barsoum Z. Accuracy of computational welding mechanics methods for estimation of angular distortion and residual stresses. *Weld. World* 2019. doi:[10.1007/s40194-019-00746-9](https://doi.org/10.1007/s40194-019-00746-9).
- [56] Cho SH, Kim JW. Analysis of residual stress in carbon steel weldment incorporating phase transformations. *Sci. Technol. Weld. Join.* 2002;7(4):212-16. doi:[10.1179/13621710225004257](https://doi.org/10.1179/13621710225004257).
- [57] Capracci JD, Fu G, Carrara JF, Remes H, Shin SB. A benchmark study of uncertainty in welding simulation. *Mar. Struct.* 2017;56:69-84. doi:[10.1016/j.marstruc.2017.07.005](https://doi.org/10.1016/j.marstruc.2017.07.005).
- [58] Wikander L, Karlsson L, Nasstrom M, Webster P. Finite element simulation and measurement of welding residual stresses. *Model. Simul. Mater. Sci. Eng.* 1994;2(4):845-64. doi:[10.1088/0965-0393/2/4/004](https://doi.org/10.1088/0965-0393/2/4/004).
- [59] Wohlfahrt H, Nitschkepagel T, Dilger K, Siegeln D, Brand M, Sakkiettibutra J, et al. Residual stress calculations and measurements — review and assessment of the iiw round robin results. *Weld. World* 2012;56(9-10):120-40. doi:[10.1007/bf03321387](https://doi.org/10.1007/bf03321387).
- [60] Sepe R, Wiebesiek J, Sonsino CM. Numerical and experimental validation of residual stresses of laser-welded joints and their influence on the fatigue behaviour. *Fatigue Fract. Eng. Mater. Struct.* 2019;43(6):1126-41. doi:[10.1111/ffe.13180](https://doi.org/10.1111/ffe.13180).